EES Batteries

PAPER

View Article Online
View Journal

Cite this: DOI: 10.1039/d6eb00039h

Substrate-dependent calcium plating on late-transition and p-block metals

Wouter Monnens, [a] Robert Markowski,[b] Andrii Kachmar,[b] Zhenyu Zhou,[a] Roy Heyns,[c] Alexandru Vlad, [b] Koen Binnemans [c] and Jan Fransaer *[a]

Received 16th February 2026,
Accepted 23rd February 2026

DOI: 10.1039/d6eb00039h

rsc.li/EESBatteries

Calcium plating on late-transition and p-block metal substrates was studied in a $Ca(BH_4)_2$/THF electrolyte. Electrochemical measurements and post-deposition analysis show clear differences between substrates in both electrochemical response and deposit morphology. On In, Pb and Ga, limited alloy formation is observed at potentials more positive than Ca metal plating. On Cu, Au, Al, and Zn, Ca plating proceeds without observable alloy formation. Short-time galvanostatic experiments reveal differences in the size and spatial distribution of Ca nuclei formed on different substrates. Cycling experiments yield distinct voltage profiles for Pb and In, but these results are discussed separately from the short-time plating experiments.

Broader context

Calcium-based batteries are attracting growing interest as potential alternatives to lithium-ion technology due to their elemental abundance, low cost, and high volumetric capacity. While the majority of research thus far has focussed on electrolyte development to enable reversible calcium plating and stripping, the role of the negative electrode substrate has received comparatively little attention. Interfacial interactions between plated calcium and the current collector can strongly influence nucleation behaviour, deposit morphology, and electrochemical reversibility, yet remain poorly understood. By systematically comparing early-stage calcium plating on a range of late-transition and p-block metal substrates, this work provides experimental insight into how substrate chemistry governs alloy formation, nucleation density, and interfacial polarization. These observations contribute to a more detailed understanding of calcium–substrate interactions and may help inform future studies on electrode and interface design in calcium-based battery systems.

1. Introduction

Calcium (Ca) has attracted increasing attention as a negative electrode material for next-generation rechargeable batteries due to its Earth abundance, low cost, and divalent charge.[1] Ca exhibits a negative standard reduction potential (−2.87 V *vs.* SHE) with a high theoretical volumetric capacity (2073 mAh cm^{-3}) but diminished theoretical gravimetric capacity (1337 mAh g^{-1}), making it attractive for stationary and large-scale energy storage applications.[2] While Ca's gravimetric energy density is lower than that of Li, its high abundance (fifth most common element in the Earth's crust) and favourable volumetric characteristics make Ca-based batteries a promising option among post-Li battery systems.[3]

Early work on Ca metal batteries identified severe passivation of Ca surfaces in several non-aqueous electrolytes, which inhibited reversible Ca plating and stripping.[4] Subsequent studies demonstrated that borohydride-based electrolytes based on $Ca(BH_4)_2$ in tetrahydrofuran (THF) enable quasi-reversible Ca deposition at room temperature.[5] Although alternative electrolytes have since been developed that have broader operational voltage windows, borohydride-based systems remain the highest-performing to date in terms of coulombic efficiency (CE).[6–8] Nevertheless, CE and cycle life remain severely limited, mainly due to the formation of an unstable solid–electrolyte interphase (SEI).[9–18]

In contrast, the role of the negative electrode itself—specifically the choice of current collector and its interaction with plated Ca—has received comparatively little attention. In Li- and Na-metal batteries, substrate engineering and surface energetics are known to strongly influence the nucleation overpotential, deposit morphology, and cycling stability.[19–21]

For Ca metal, similar concepts are expected to be relevant but remain far less explored, as most prior work has focused on electrolyte development and coordination chemistry.[8,11,15–18,22] However, Ca electrochemistry in the

[a]KU Leuven, Department of Materials Engineering, Kasteelpark Arenberg 44, P. O. box 2450, B-3001 Leuven, Belgium. E-mail: Jan.fransaer@kuleuven.be
[b]UC Louvain, Institute of Condensed Matter and Nanosciences, Place L. Pasteur 1, Lavoisier Building, B-1348 Louvain-la-Neuve, Belgium
[c]KU Leuven, Department of Chemistry, Celestijnenlaan 200F, P.O. box 2404, B-3001 Leuven, Belgium

reported electrolytes differs from that of alkali metals in several important aspects. Reported Ca plating processes are often associated with large polarization and limited reversibility, and are strongly influenced by electrolyte stability and interfacial effects.[8,16,17,22]

Several late-transition and p-block metals are known to form thermodynamically stable alloys with Ca, and both computational studies and limited experimental work suggest that Ca incorporation into such substrates may be possible during electrochemical reduction.[23,24] Nevertheless, experimental insight into how substrate chemistry influences the early electrochemical response and deposit morphology during Ca plating remains scarce.

In this work, we present an experimental comparison of Ca electrochemistry and plating on a range of late-transition and p-block metal substrates (Zn, Cu, Al, Au, Bi, In, Pb, and Ga) using a $Ca(BH_4)_2$/THF electrolyte. However, the study is limited to early-stage Ca plating under polarized conditions, partly competing with SEI formation and possible electrolyte degradation, and low Ca loadings, and therefore primarily probes initial interfacial responses rather than equilibrium behaviour or long-term cycling performance.

2. Experimental section

2.1 Materials and chemicals

Ca disks with a diameter of 5 mm and a thickness of 0.5 mm were purchased from ZZK Materials INC (Zhuzhou City, Hunan Province, China). Silver (Ag, wire, >99.9 %), Gallium (Ga, lumps/liquid, >99.99%), aluminium (Al, foil (0.25 mm thickness), 99.999%), bismuth (Bi, foil (0.25 mm thickness), >99.9%), calcium borohydride bis(tetrahydrofuran) ($Ca(BH_4)_2{\cdot}2C_4H_8O$), tetrabutylammonium tetrafluoroborate ($TBABF_4$, 99%) and tetrahydrofuran (THF, >99.9%, anhydrous) were purchased from Sigma-Aldrich (Diegem, Belgium). Zinc (Zn, foil (0.25 mm thickness) > 99.99%), indium (In, lumps, >99.999%) and lead (Pb, foil of 0.25 mm thickness, >99.8%) were received from Umicore (Olen, Belgium). Gallium was melted on a glass slit at 40 °C and cast into disks with a diameter of 10 mm and an approximate thickness of 0.25 mm, whereas indium chunks were cut and press-rolled into sheets with approximate thicknesses of 0.25 mm. 10 mm diameter disks were punched from all metal sheets. All other chemicals were used as received and were always stored in an argon-filled glovebox.

2.2 Electrochemical characterization

All electrochemical measurements and coin cell assembly were performed inside an argon (Ar)-filled glovebox with water and oxygen concentrations around 1 ppm. Cyclic voltammograms (CV) were recorded using an Autolab PGSTAT302N (Metrohm, Kontich Belgium). CVs were always started at the open circuit potential (OCP) and scanned first towards cathodic overpotentials. They were recorded using three-electrode setups with a Ca counter electrode and a silver sulfide/silver (Ag_2S/Ag) reference electrode which has been proven to be a reliable reference electrode for measurements in non-aqueous electrolytes.[25,26] This electrode consisted of a glass tube with a frit filled with THF containing 0.5 M of $TBABF_4$, into which an Ag_2S-coated Ag wire was immersed. The Ag_2S-coated wire was prepared by reacting a polished Ag wire with sublimated sulfur (S) in a closed cell at 130 °C. In a solution of 1.5 M of $Ca(BH_4)_2$ in THF, a Ca bulk electrode exhibited a stable potential of −2.32 V *vs.* Ag_2S/Ag. The (post-)transition-metal electrodes were mounted in a small sample holder featuring a spherical aperture with an exposed area of 0.125 cm^2, which was in contact with the electrolyte. Before any electrochemical measurement, dry polishing of Ca was manually performed using 4000p sandpaper inside the glovebox. The (post)-transition metal electrodes were washed with either 0.1 M of H_2SO_4 or 0.25 M of HNO_3, followed by a demineralized water rinse and an acetone rinse to remove native oxides prior to transfer inside the glovebox. Only Ga electrodes did not receive any oxide removal step, since this would change the morphology from cast electrode films to droplets due to the high surface tension of the neat metal. For plating and cycling experiments, CR2032-type coin cells were assembled with a Ca metal disk as counter and pseudo-reference electrode and a In, Pb, cast Ga, Al, Bi, Zn, Cu or Au metal disk (10 mm diameter, 0.25 mm thickness) as working electrode. Au electrodes were sputtered on stainless steel disks with diameters of 10 mm. For the short-time (3.6 and 36 s) plating experiments, a Celgard™ separator was used which was soaked with 20 µl of electrolyte, whereas for the CVs and cycling tests, a glass fibre separator was used which was soaked with 100 µl of electrolyte. The Celgard™ separator could consistently be removed without tearing the Ca deposits off the working electrodes, yet would be penetrated, during CVs and cycling tests where a larger amount of Ca would be deposited, caused by localized, non-uniform deposited protruding Ca crystallites. It was found that the thicker glass fibre separator was more suitable for the latter measurements. Yet, removal of this separator typically led to partial removal of the plated Ca as well. The galvanostatic charge–discharge tests were performed on a Neware battery testing system (Shenzhen Neware Electron. Co. Ltd, China). 1 mA cm^{-2} was applied for 30 minutes during plating. A cut-off potential of −1.0 V *vs.* Ca pseudo RE was set. Consequently, 1 mA cm^{-2} was applied for stripping, with a set cut-off of +1.0 V *vs.* Ca pseudo RE. CEs were calculated by dividing the accumulated plating charge by the accumulated stripping charge.

2.3 Characterization

After electrochemical measurements, the electrode materials were carefully removed from the measurement setups or coin cells, rinsed with pure THF and dried in a vacuum chamber. The morphology of the prepared deposits was studied by scanning electron microscopy (SEM) (FEI, Nova 600 Nanolab). Samples were transferred in an Ar-filled container from the glovebox to the microscope and quickly transferred inside to minimize exposure to ambient atmosphere. Energy-dispersive

X-ray spectroscopy (EDX) with an octane elite super silicon drift detector (Ametek EDAX) was used for elemental analysis. For all measurements, the acceleration voltage was 10 keV. X-ray diffraction (XRD) was measured using a Bruker D2 Phaser X-ray diffractometer. Samples were encased in Kapton tape inside the glovebox and kept in an Ar-filled container filled until the start of the measurement. Data processing was realized *via* the DIFFRAC.EVA VER.5 2019 in the DIFFRAC.SUITE.EVA program package and the ICDD PDF4 + 2021 database.

3. Discussion

3.1 Cyclic voltammetry

CVs were recorded using 1.5 M of $Ca(BH_4)_2$ in THF at 21 °C for eight different metal electrodes, including In, Pb, Ga, Bi, Cu, Al, Au and Zn. The resulting 1st (red dotted line) and 10th cycle (black full line) for each electrode is shown in Fig. 1. The measurements were performed in a three-electrode configuration using a stable Ag_2S/Ag reference electrode; nevertheless, the measured potentials remain strongly influenced by interfacial polarization and kinetic limitations associated with Ca reduction, SEI formation, and therefore should not be interpreted as equilibrium thermodynamic potentials. All CVs show a cathodic feature and an anodic peak, which are ascribed to the reduction of Ca^{2+} to Ca metal and the stripping of Ca, respectively. For all recorded CVs, a clear positive shift in bulk plating onset potential is seen in the 10th cycle as compared to the 1st cycle, whereas the stripping onset potential remains the same. The extent of the shift in plating onset varies among the metal electrodes. This shift might be because not all Ca is stripped after each cycle (CEs of the CVs are shown in Fig. S1, SI). As a result, in the 10th cycle, nucleation likely occurs partially on the accumulated unstripped Ca, which shifts the onset potential to more positive values compared to the onset potentials observed in the 1st cycle. However, no plating onset is observed at potentials corresponding to the apparent onset of bulk Ca plating (0.0 V *vs.* Ca pseudo RE under the present conditions, −2.32 V *vs.* Ag_2S/Ag), as the electrode surface is likely not fully covered with Ca. In addition, the presence of a SEI requires a cathodic overpotential to initiate Ca plating.[16] Interestingly, the observed current densities are higher in the 10th cycle. However, the ratio of the cathodic to anodic current density (*i.e.*, CE) remains relatively consistent for the 1st and 10th cycle. In all CVs, the cathodic current densities in the 10th cycle exhibit clear nucleation loops and show peak currents, which are indicative of metal plating in a diffusion-controlled regime. There are large differences in the increase of current densities from the 1st cycle to the 10th cycle for the different metals. The largest increase is observed for Al and Ga, followed by a slightly smaller increase for Cu, Bi, and Zn. In contrast, In, Pb, and Au show only minor changes in current density between cycles. The comparatively low cathodic currents observed for Al and Ga during the 1st cycle may be attributed to the presence of native oxide layers, which can form even after polishing in an argon-filled glovebox with oxygen levels as low as 1 ppm. Such surface oxides are expected to exhibit sluggish Ca plating kinetics relative to the bare metal and may additionally undergo galvanic exchange reactions with Ca, leading to CaO formation. Differences in current evolution may also reflect variations in the morphology of the developing Ca deposits. Large increases in current density are consistent with the formation of deposits with high effective surface area, whereas more modest increases suggest thinner or smoother deposits. These morphological differences likely arise from variations in Ca–substrate interactions and may promote distinct growth modes, such as Volmer–Weber-type growth.

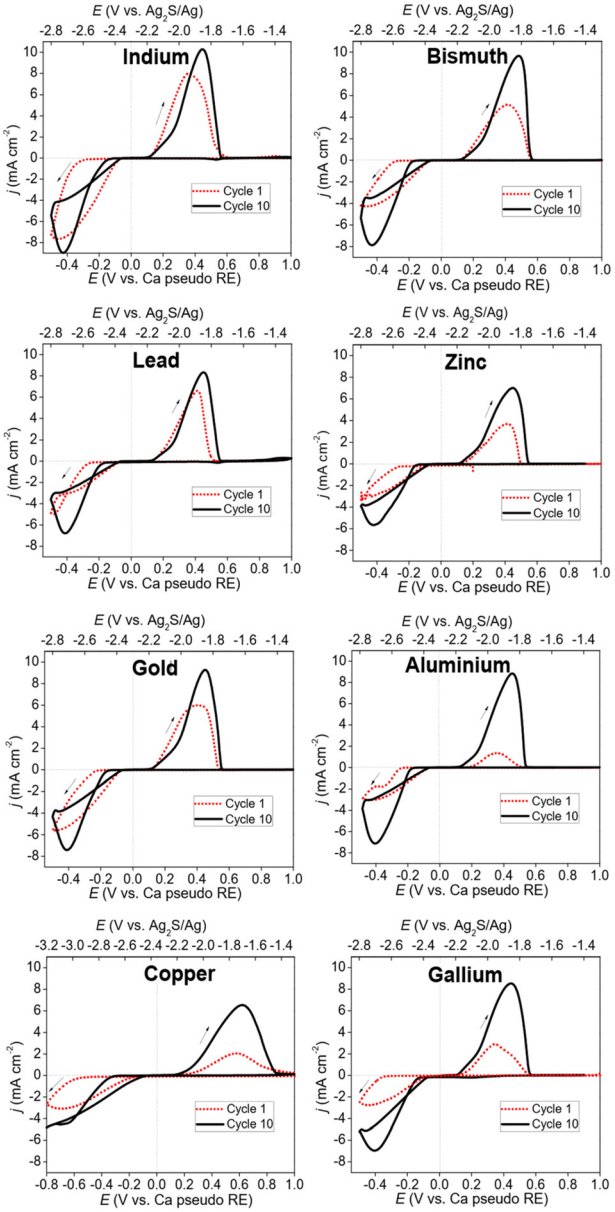

Fig. 1 CVs (1st and 10th cycle) recorded on various metal electrodes using an electrolyte composed of 1.5 M of $Ca(BH_4)_2$ in THF at 21 °C. The scan rate was 1 mV s^{-1}.

Notably, despite these differences, all CVs exhibit broadly similar shapes and comparable total charge.

At first glance, none of the deposition processes appear fully reversible, as the cathodic current density in the reverse scan nearly equals zero for more than 100 mV before becoming anodic. Closer inspection of the first-cycle CVs using a magnified current density scale (Fig. 2), however, reveals additional features. For In, Pb, Bi, and Ga, a reduction current is detected at substantially positive apparent potentials, extending up to +1.0 V *vs.* Ca pseudo RE (−1.32 V *vs.* Ag_2S/Ag). At these potentials, the current densities are very low and are therefore tentatively attributed to parasitic processes such as the reduction of residual impurities or native oxides. From approximately +0.5 V *vs.* Ca pseudo RE (−1.82 V *vs.* Ag_2S/Ag), the cathodic current increases gradually and, for In and Pb, develops into well-defined peak features at +0.36 V and +0.48 V *vs.* Ca^{2+}/Ca, respectively. Upon further polarization, the current rises sharply at −0.27 V (In), −0.23 V (Pb), −0.25 V (Bi), and −0.33 V (Ga) *vs.* Ca pseudo RE, corresponding to the onset of dominant Ca metal plating. According to the binary phase diagrams, all metal electrodes exhibit the tendency to form alloys with Ca at room temperature.[27,28] The exact nucleation and growth mechanism is likely complex and cannot be determined reliably from CV data alone. Nevertheless, several features can be inferred from the observed voltammograms. For In and Pb electrodes, cathodic currents appear already at relatively positive potentials, starting at approximately +0.5 V *vs.* Ca pseudo RE (−1.82 V *vs.* Ag_2S/Ag) and forming well-defined peaks. These cathodic features occur at substantially more positive apparent potentials than the onset of bulk Ca plating and are therefore inconsistent with simple metallic Ca plating under the present conditions. Moreover, they also cannot be explained by classical underpotential deposition, since the associated charges (1.4 mC for In and 1.0 mC for Pb) are much larger than those expected for monolayer formation. These features are instead interpreted as being consistent with near-surface Ca incorporation into the substrate, likely involving alloying reactions that occur concurrently with other interfacial processes. Under the present experimental conditions, alloy growth is expected to be non-uniform and limited to a shallow near-surface region. This is because Ca transport into the metal is governed by solid-state diffusion, which is slow at room temperature and over the timescale of the CV experiment. The proposed alloy-formation process can be described by:

$$x\mathrm{Ca}^{2+} + 2x\mathrm{e}^{-} + y\mathrm{M} \rightarrow \mathrm{Ca}_x\mathrm{M}_y \quad (1)$$

with x and y representing the stoichiometric coefficients for Ca and M (M = Pb or In). Reported Gibbs free energies of formation (ΔG_f) for Ca–In and Ca–Pb alloys indicate that Ca incorporation into these metals is thermodynamically favourable. Such alloy formation has been widely reported for other s-block metal systems, including Li, Na, K, and Mg.[29–32] Table 1 summarizes stable Ca–In and Ca–Pb alloy phases reported in the literature together with their corresponding ΔG_f values. For completeness, these thermodynamic data can be expressed in terms of an *idealized* shift in reduction potential associated with alloy formation according to:

$$\Delta E = E_{\mathrm{alloy}} - E_{\mathrm{Ca}^{2+}/\mathrm{Ca}} = -\frac{\Delta G_f(\mathrm{Ca}_x\mathrm{M}_y)}{nxF} \quad (2)$$

where ΔE represents the shift in reduction potential associated with alloying, F the Faraday coefficient (96 485.3 C mol^{-1}) and

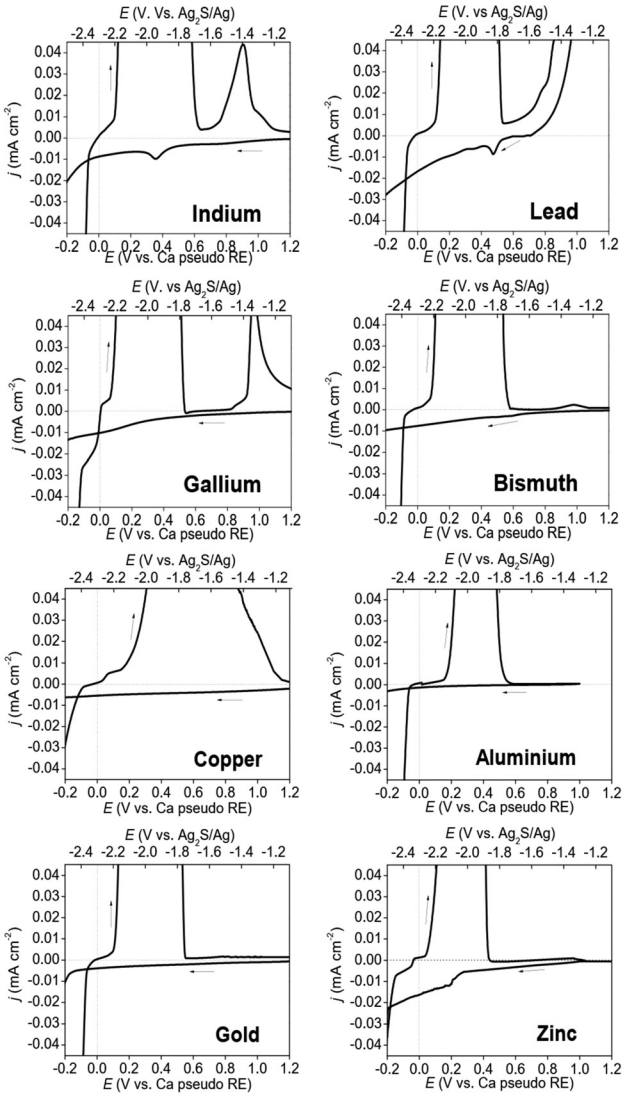

Fig. 2 Magnified CVs (1st cycle) recorded on the eight metal electrodes using an electrolyte composed of 1.5 M of $Ca(BH_4)_2$ in THF at 21 °C. The scan rate was 1 mV s^{-1}.

Table 1 Stable Ca–In and Ca–Pb alloy phases, their respective ΔG_f values (for 298.15 K) and their calculated shift in reduction potential

System	Phase	ΔG_f (kJ mol^{-1})	ΔE (V)	Temperature (K)
Ca–In	Ca_3In	−54.5[33]	0.09	298.15
	CaIn	−61.7[33]	0.32	298.15
	$CaIn_2$	−55.8[33]	0.29	298.15
Ca–Pb	Ca_2Pb	−66.9[34]	0.17	298.15
	Ca_5Pb_3	−66.7[34]	0.07	298.15
	CaPb	−55.2[34]	0.29	298.15
	$CaPb_3$	−32.1[34]	0.17	298.15

n the number of electrons involved in the reduction reaction (n = 2). While this expression provides a thermodynamic reference framework, it assumes equilibrium bulk phase formation and neglects interfacial polarization, kinetic limitations, and concurrent interfacial reactions. The calculated theoretical ΔE values (0.07–0.32 V, depending on alloy phase) should therefore be interpreted only as *order-of-magnitude indicators* of the thermodynamic driving force for Ca incorporation, rather than quantitative predictors of the experimentally observed CV features. Under the present experimental conditions, the voltammetric response reflects kinetically controlled, near-surface processes that are strongly influenced by polarization and SEI formation. As a result, direct numerical correspondence between calculated alloying potentials and experimental onset potentials is not expected.

At more negative apparent overpotentials, a nucleation loop is observed, which is assigned to the onset of dominant metallic Ca plating occurring on an evolving interfacial layer. Notably, the presence of the near-surface alloy layer does not drastically reduce the nucleation overpotential, typically seen for Li- and Na-alloying electrodes.[35,36] This suggests that the electrochemical response is dominated by SEI formation (on the interfacial alloy) and electrolyte-limited kinetics, rather than efficient alloy-mediated nucleation of metallic Ca. In the reverse scan, the CVs recorded on In, Pb, and Bi cross the apparent Ca-pseudo potential under the present conditions (−2.32 V *vs.* Ag_2S/Ag) and become anodic, exhibiting a small shoulder-like feature before the current increases more steeply at approximately +0.1 V *vs.* Ca pseudo RE (−2.22 V *vs.* Ag_2S/Ag). The reduced current density associated with these shoulder-like features is consistent with partial interfacial passivation, likely arising from a metastable SEI that initially hampers Ca stripping.[17] Upon further anodic polarization, the current density increases sharply, indicating bulk Ca stripping. Following the primary stripping peak, In, Pb, Ga, and Bi electrodes exhibit an additional anodic feature, although it is very small in the case of Bi. This feature is tentatively assigned to Ca dealloying from near-surface Ca_xM_y regions formed during prior reduction. For In, the charge associated with this secondary anodic feature (5.9 mC) exceeds that of the initial cathodic alloy-related peak, suggesting that additional alloying into the near-surface region occurs during metallic Ca plating. A similar trend is observed for Pb, where the alloy-related stripping charge reaches 11.6 mC. For Ga, no distinct alloy-deposition peak is observed in the first cycle; instead, a broad shoulder-like cathodic feature is present. Nevertheless, the pronounced anodic feature observed during stripping indicates that Ca–Ga alloying occurs over an extended potential range, encompassing both the initial reduction feature and the subsequent metallic Ca plating regime. As shown in Fig. S2 (SI), magnified CVs of the 10th cycle reveal that alloy-related cathodic features become more pronounced for Ga and are amplified for In and Pb. This evolution is likely associated with surface roughening and an increase in electrochemically active area resulting from repeated alloying and dealloying. While the second anodic peak related to alloy stripping persists for In and Pb, it largely disappears for Ga, suggesting that the formed Ca–Ga alloys do not de-alloy within the investigated potential window. In contrast, the magnified CVs of Cu, Al, Au, and Zn (Fig. 2) display different behaviour. Only Zn exhibits a cathodic feature at positive apparent overpotentials that may indicate alloy formation. On all four CVs, nucleation loops are observed, indicating bulk Ca plating. The subsequent anodic currents remain low for several tens of millivolts before increasing sharply, with only Cu exhibiting a weak shoulder-like feature prior to bulk stripping. Notably, none of these substrates display a secondary anodic feature attributable to de-alloying, indicating that alloy formation is negligible or absent under the present conditions.

3.2 Galvanostatic deposition and morphology of Ca

Ca plating was carried out using 1.5 M of $Ca(BH_4)_2$ in THF on the eight metal electrodes by applying −1 mA cm^{-2} for 36 s. The corresponding voltage transients are shown in Fig. 3. They exhibit a distinct nucleation overpotential (η_n), representing the initial voltage spike that onsets Ca nucleation. This is fol-

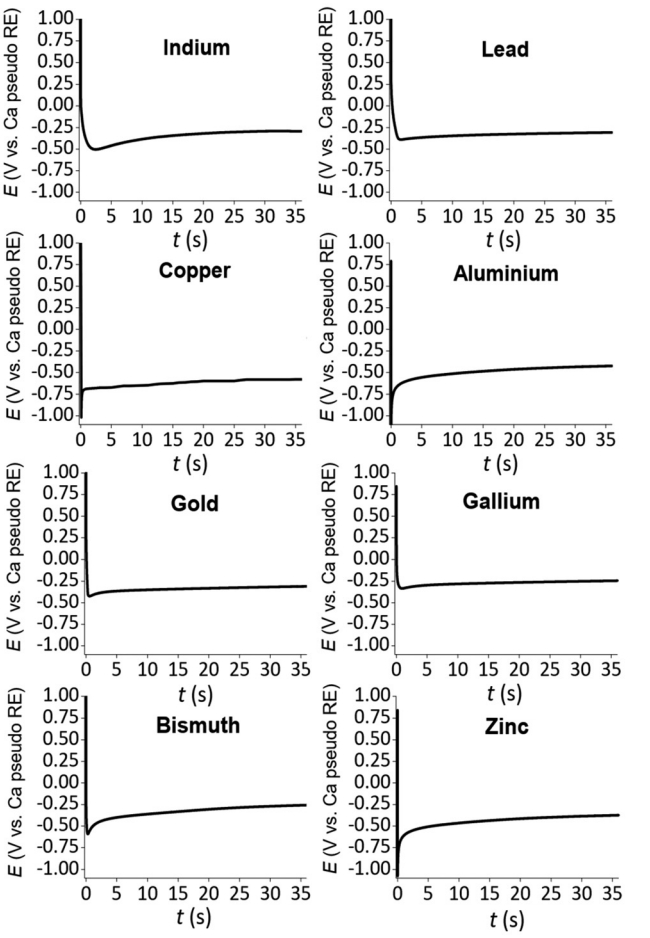

Fig. 3 Voltage *vs.* time transients of Ca plating recorded on various metal electrodes. A current density of −1 mA cm^{-2} was applied for 36 s (capacity density of 0.01 mAh cm^{-2}) at 21 °C. The theoretical thickness of the deposits is 49 nm, assuming 100% cathodic current efficiency and uniform coverage.

lowed by a plateau overpotential (η_p) attributed to the Ca growth after nucleation. The magnitude of both η_n and η_p varies among the electrode types. Al, Cu and Zn exhibit the largest values, implying the need for sufficiently high cathodic overpotentials to drive the nucleation and growth of Ca. Transients for In, Pb, Au and Ga show lower values, with η_n only being slightly larger than η_p. For In, Pb and to a lesser extent for Ga, a minor time delay is observed prior to reaching η_n. Analogously to the observations in the magnified CVs, this initial region might be due to alloy deposition occurring at positive overpotentials as compared to 0.0 V *vs.* Ca pseudo RE.

SEM images of the according deposits are shown in Fig. 4. For none of the cases, Ca fully covered the surface of the metal substrates. However, for In, Pb and Au, the deposits clearly exhibit higher coverage. For Au, this has been reported earlier by Yao *et al.*[23] The deposit on In seems slightly thicker than on Pb and Au. For the other substrates, Ca deposited as isolated islands. For Cu and Al, they are especially large and rough, representing cauliflower-like structures. On Ga, Bi and Zn, denser and smaller island deposits formed. While it is important to consider that the deposits on all electrodes might be altered through oxidation occurring during the brief exposure to ambient atmosphere during sample transfer to the SEM chamber, it is presumed that this did not cause any substantial changes in the observed morphologies. Consequently, the observed morphologies for In, Pb, and Au appear slightly less rough than those for other metals as the small interface area with the electrolyte reduces parasitic reactions with solution components, thereby reducing the consumption of active material. This typically results in improved CE and enhanced cyclability. Yet, it must be stated for In, Pb and Au, growth remains localized and does not proceed fully laterally, preventing coalescence into a continuous thin film. Fig. 5 presents the elemental EDX maps and corresponding SEM images of the deposits generated by applying −1 mA cm^{-2} for 36 s, with the EDX spectra provided in Fig. S3–S10 (SI). The deposits are predominantly composed of pure Ca, except for the Ga deposit where both Ca and Ga are detected, suggesting that the deposit consisted of Ca–Ga alloys. To verify the potential formation of alloys with Ga, as well as with In and Pb during alloy deposition (and Ca metal plating), X-ray diffraction (XRD) diffractograms of the deposits were measured that were prepared by applying −1 mA cm^{-2} for 360 s. XRD diffractograms (Fig. S11, SI) reveal weak reflections that can be assigned to Ca–In, Ca–Pb, and Ca–Ga alloy phases. The low intensity and

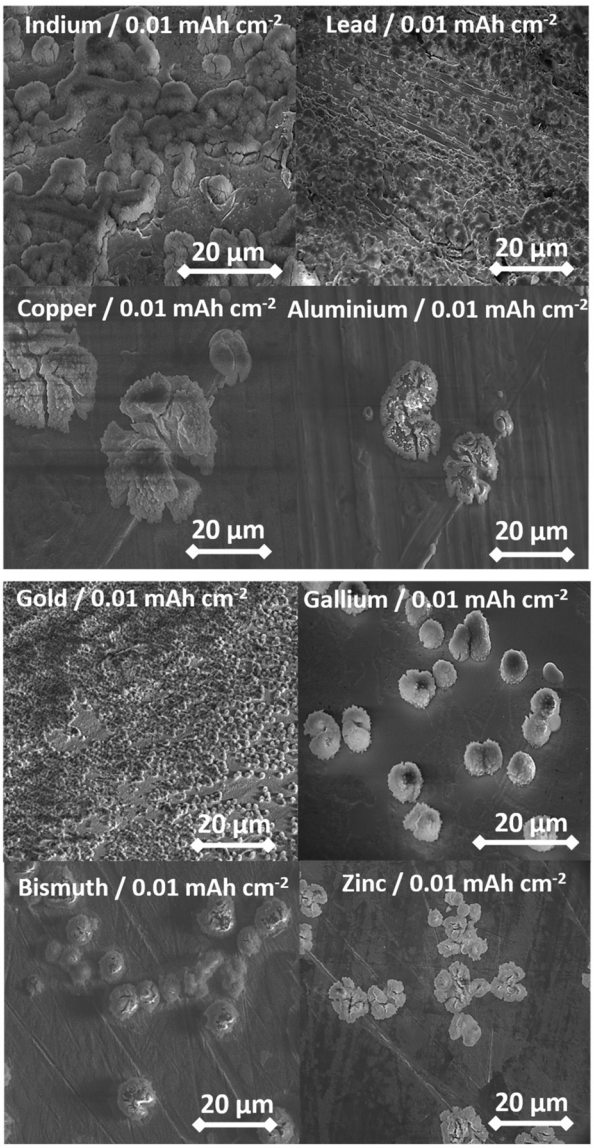

Fig. 4 SEM images of Ca deposits on the metal electrodes. The images were taken under a 35° angle, with an applied acceleration voltage of 10 keV.

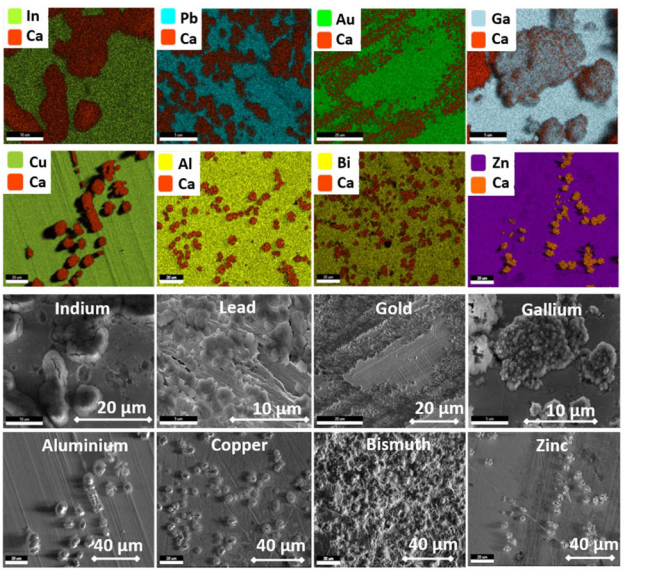

Fig. 5 Top-down EDX elemental maps and corresponding SEM images of Ca deposits on the metal electrodes. Ca deposits were generated by applying a current density of −1 mA cm^{-2} for 36 s (capacity density of 0.01 mAh cm^{-2}) at 21 °C. The applied acceleration voltage was 10 keV.

broadening of these reflections indicate that alloy formation is confined to a thin near-surface region rather than extending deeply into the metal substrates. Some alloy-related reflections may fall below the detection limit of laboratory XRD.

3.3 Nucleation of Ca on In, Pb, Cu and Al

Galvanostatic deposition of Ca was performed on alloying In and Pb, and non-alloying Cu and Al using 1.5 M of $Ca(BH_4)_2$ in THF at a current density of −1 mA cm^{-2} for 3.6 s. It is emphasized that the applied Ca loadings are extremely low. Under these conditions, the electrochemical response primarily reflects nucleation and interfacial processes. The resulting voltage transients are shown in Fig. 6(a). For In and Pb, the transients display an initial region of gradual voltage evolution at positive apparent overpotentials, followed by a nucleation feature at −0.57 V and −0.41 V, respectively. In both cases, the nucleation overpotential (η_n) is similar in magnitude to the subsequent plateau overpotential (η_p), as indicated by the red dotted line. This indirectly indicates alloy formation prior to Ca plating. Similar galvanostatic signatures have been reported for Li and Na deposition on alloy-forming substrates, although direct analogy is complicated by the stronger polarization and slower kinetics characteristic of Ca electrochemistry.[32,37] In contrast, voltage transients recorded on Cu and Al exhibit a sharp and pronounced η_n peak that develops almost instantaneously upon current application. Both η_n and η_p are substantially larger for Cu and Al than for In and Pb, consistent with more polarized Ca nucleation and growth under the present conditions. Fig. 6(b) presents top-down SEM images of the Ca nuclei. Clear differences in nucleation morphology are observed between the substrates. In and Pb exhibit a high density of nanoscale nuclei, with individual Ca crystallites appearing below the reliable size resolution of SEM. In contrast, Ca nuclei on Cu and Al are more thinly distributed and tend to cluster into fewer, larger features. While the absolute size of individual nuclei cannot be quantified accurately from SEM, the observed trends indicate different nucleation densities across the substrates. Duplicate SEM images are provided in Fig. S12 and S13 (SI). For all substrates, the apparent thickness of the deposits exceeds the average value calculated from the passed charge, reflecting highly localized nucleation and non-uniform growth. The higher density of small nuclei observed on In and Pb suggests that the evolving substrate surface—potentially modified by alloy formation—remains a favourable site for continued Ca reduction during the earliest stages of deposition. In contrast, for Cu and Al, Ca reduction appears to proceed preferentially on existing Ca nuclei rather than on the substrate. These differences in nucleation behaviour are consistent with the more uniform deposit morphologies observed at higher Ca loadings (Fig. 5).

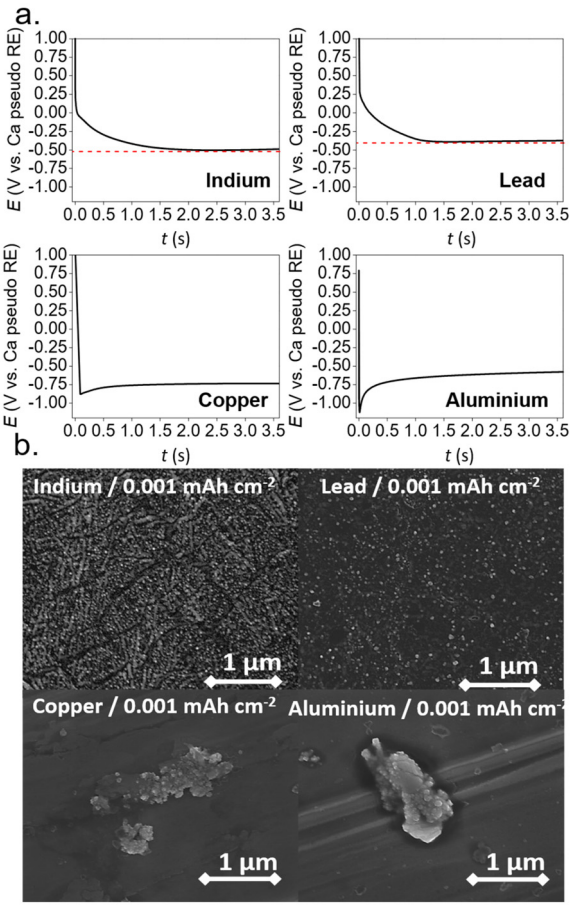

Fig. 6 (a) Voltage *vs.* time transients of Ca plating recorded on In, Pb, Cu and Al electrodes. A current density of −1 mA cm^{-2} was applied for 3.6 s (capacity density of 0.001 mAh cm^{-2}) at 21 °C. The theoretical thickness of the deposits is 4.9 nm, assuming 100% cathodic current efficiency and uniform coverage. (b) Top-down SEM images of Ca nuclei on the four electrodes. The applied acceleration voltage was 10 keV.

3.4 Cycling performance

Half-cells were assembled using either an In or Pb working electrode paired with a Ca counter electrode, and galvanostatic cycling was performed at 1 mA cm^{-2} with a fixed areal capacity density of 0.5 mAh per cm^2 per cycle. It is emphasized that the cycling data presented correspond to the best-performing cells obtained under the conditions investigated. As shown in Fig. 7(a), the voltage profiles for Ca plating and stripping on In and Pb do not exhibit well-defined, stable plateaus at fixed cathodic or anodic overpotentials. Instead, Ca plating is characterized by an initial nucleation-related feature, followed by a gradual decrease in cell voltage that evolves toward a broader plateau only at more negative overpotentials. During stripping, the voltage response shows a pronounced peak, followed by a shallow depression before the cell voltage rises abruptly to the upper cut-off potential of +1.0 V. The origin of these features cannot be determined with confidence using the present experimental setup, as the effects of interfacial polarization, SEI evolution, and electrolyte degradation cannot be separated. Cells employing Pb electrodes exhibit more stable voltage profiles and maintain reversible cycling for a larger number of cycles than those employing In electrodes. Nevertheless, as shown in Fig. 7(b), the CE remains limited for both systems, fluctuating between 70 and 80%, which is consistent with previous reports on Ca plating using borohydride-based electrolytes.[9] This limited efficiency is generally attributed to the formation of an unstable

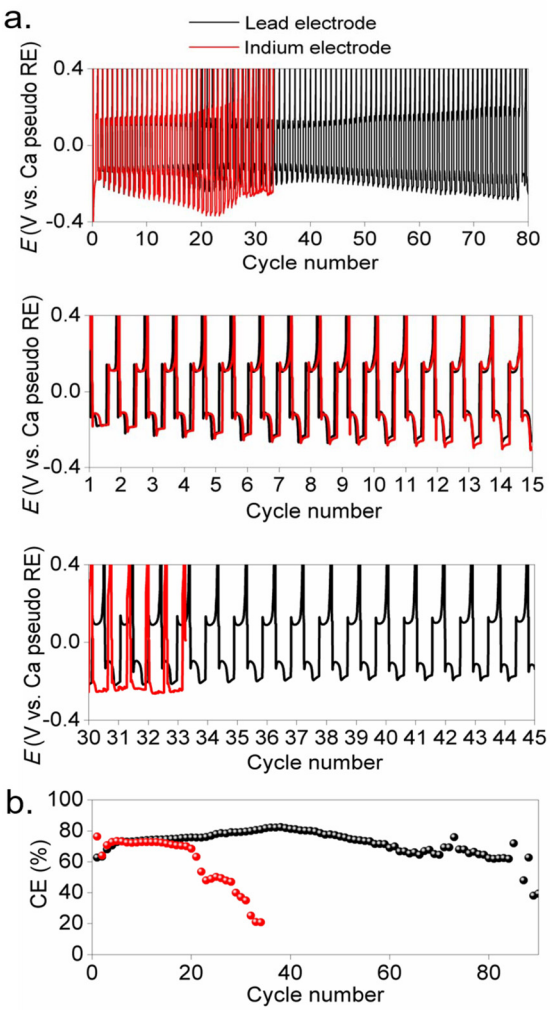

Fig. 7 (a) Cycling performance and polarization evolution for the In||Ca and Pb||Ca cells in 1.5 M of $Ca(BH_4)_2$ in THF at a current density of 1 mA cm^{-2} and a capacity density of 0.5 mAh cm^{-2}. The cells were cycled at 21 °C and the set cut-off voltage was +1.0 V *vs.* Ca pseudo RE, well below the original OCP of the cells, equalling +1.34 V *vs.* Ca pseudo RE for In||Ca and +1.55 V *vs.* Ca pseudo RE for Pb||Ca, respectively. (b) The attained CE *vs.* cycle number for the In||Ca and Pb||Ca cells.

SEI on Ca deposits, leading to continuous electrolyte decomposition, gas evolution, and progressive loss of active Ca.[17] Pb electrodes show more stable voltage profiles than In under the investigated conditions. However, the cycling behaviour reflects a different electrochemical regime than the short-time deposition experiments and should therefore not be directly correlated with the early-stage nucleation results.

4. Conclusions

This study explores the influence of metallic substrates on the early stages of Ca plating in a $Ca(BH_4)_2$/THF electrolyte. Cyclic voltammetry reveals substrate-dependent differences in electrochemical response. For In, Pb, and Ga, Ca reduction leads to alloy formation before metallic Ca plating, whereas Ca plating on Cu, Al, Au, and Zn occurs without notable alloy formation. The presence of near-surface alloys does not substantially lower the Ca plating onset potential, suggesting that interfacial polarization, the formed SEI and sluggish kinetics play an important role. Differences in substrate chemistry are also reflected in the morphology of Ca deposits formed during longer plating times (36 s) and in early nucleation behaviour at low Ca loadings. In and Pb show smaller crystallites and higher nucleation densities than Cu and Al. Cycling experiments performed at higher applied capacities show differences in voltage evolution between Pb and In. The origin of these voltage trends cannot be explained with confidence based on the present data, and the cycling results are therefore discussed separately from the short-time plating experiments.

Author contributions

Wouter Monnens: investigation, methodology, formal analysis, writing – original draft. Robert Markowski, Andrii Kachmar, Zhenyu Zhou and Roy Heyns: review, methodology, validation. Jan Fransaer, Koen Binnemans and Alexandru Vlad: review & editing, supervision, resources, project administration, methodology, funding acquisition.

Conflicts of interest

There are no conflicts to declare.

Data availability

The authors confirm that the data supporting the findings of this study are available within the article and its supplementary information (SI). Supplementary information: magnified CVs, coulombic efficiencies, EDX spectra, XRD diffractograms and size-distribution plots of Ca crystallites. See DOI: https://doi.org/10.1039/d6eb00039h.

Acknowledgements

This work was supported by the FWO and F.R.S-FNRS project ECOBAT (40007515) under the Excellence of Science (EOS) program.

References

1 A. Ponrouch and M. R. Palacín, *Philos. Trans. R. Soc., A*, 2019, **377**, 20180297.
2 A. Bard, *Standard potentials in aqueous solution*, Wiley & Sons, Routledge, 2017.
3 W. M. Haynes, *CRC handbook of chemistry and physics*, CRC press, Boca Raton, 2016.

4 D. Aurbach, R. Skaletsky and Y. Gofer, *J. Electrochem. Soc.*, 1991, **138**, 3536.
5 D. Wang, X. Gao, Y. Chen, L. Jin, C. Kuss and P. G. Bruce, *Nat. Mater.*, 2018, **17**, 16–20.
6 Z. Li, O. Fuhr, M. Fichtner and Z. Zhao-Karger, *Energy Environ. Sci.*, 2019, **12**, 3496–3501.
7 J. Liang, M. Wang, S. Zhu, D. Zhu, R. Wang, J. Wang, L. Cui, M. Huang, W. Zhang and Q. An, *Angew. Chem., Int. Ed.*, 2025, **64**, e202502729.
8 T. Pavčnik, J. D. Forero-Saboya, A. Ponrouch, A. Robba, R. Dominko and J. Bitenc, *J. Mater. Chem. A*, 2023, **11**, 14738–14747.
9 Y. Jie, Y. Tan, L. Li, Y. Han, S. Xu, Z. Zhao, R. Cao, X. Ren, F. Huang and Z. Lei, *Angew. Chem., Int. Ed.*, 2020, **59**, 12689–12693.
10 N. T. Hahn, J. Self, K. S. Han, V. Murugesan, K. T. Mueller, K. A. Persson and K. R. Zavadil, *J. Phys. Chem. B*, 2021, **125**, 3644–3652.
11 N. T. Hahn, J. Self, T. J. Seguin, D. M. Driscoll, M. A. Rodriguez, M. Balasubramanian, K. A. Persson and K. R. Zavadil, *J. Mater. Chem. A*, 2020, **8**, 7235–7244.
12 A. T. Landers, J. Self, S. A. McClary, K. J. Fritzsching, K. A. Persson, N. T. Hahn and K. R. Zavadil, *J. Phys. Chem. C*, 2023, **127**, 23664–23674.
13 C. Kiesl, R. Böck, H. Kaßner, J. Häcker, M. Kögel, T. Sörgel and Ş. Sörgel, *Nanomaterials*, 2025, **15**, 454.
14 S. A. McClary, D. M. Long, A. Sanz-Matias, P. G. Kotula, D. Prendergast, K. L. Jungjohann and K. R. Zavadil, *ACS Energy Lett.*, 2022, **7**, 2792–2800.
15 A. Sanz Matias, F. Roncoroni, S. Sundararaman and D. Prendergast, *Nat. Commun.*, 2024, **15**, 1397.
16 A. M. Melemed and B. M. Gallant, *J. Electrochem. Soc.*, 2020, **167**, 140543.
17 A. M. Melemed, D. A. Skiba, K. S. Jiang, G. H. Byun and B. M. Gallant, *Electrochim. Acta*, 2025, 146170.
18 A. M. Melemed, D. A. Skiba and B. M. Gallant, *J. Phys. Chem. C*, 2022, **126**, 892–902.
19 D. Petersen, M. Gronenberg, G. Lener, E. P. M. Leiva, G. L. Luque, S. Rostami, A. Paolella, B. J. Hwang, R. Adelung and M. Abdollahifar, *Mater. Horiz.*, 2024, **11**, 5914–5945.
20 A. Dandriyal, S. Patil, J. MacLeod, D. Golberg, C. Sudakar and D. Dubal, *Small*, 2025, **21**, e08811.
21 W.-J. Zhang, *J. Power Sources*, 2011, **196**, 877–885.
22 A. M. Melemed, D. A. Skiba, K. J. Steinberg, K.-H. Kim and B. M. Gallant, *J. Phys. Chem. C*, 2023, **127**, 19886–19899.
23 Z. Yao, V. I. Hegde, A. Aspuru-Guzik and C. Wolverton, *Adv. Energy Mater.*, 2019, **9**, 1802994.
24 Z. Zhao-Karger, Y. Xiu, Z. Li, A. Reupert, T. Smok and M. Fichtner, *Nat. Commun.*, 2022, **13**, 3849.
25 C. Horwood and M. Stadermann, *Electrochem. Commun.*, 2018, **88**, 105–108.
26 J. M. Shellhamer, P. A. Chando, S. Pathreeker, X. Wang and I. D. Hosein, *J. Phys. Chem. C*, 2023, **127**, 19900–19905.
27 V. N. Volodin and Yu. Zh. Tuleushev, *Russ. J. Phys. Chem. A*, 2020, **94**, 1300–1305.
28 B. Predel, *Phase Equilibria, Crystallographic and Thermodynamic Data of Binary Alloys Ca-Cd – Co-Zr*, Springer, Heidelberg, 1993.
29 H. Liu, X.-B. Cheng, J.-Q. Huang, S. Kaskel, S. Chou, H. S. Park and Q. Zhang, *ACS Mater. Lett.*, 2019, **1**, 217–229.
30 J. Niu, Z. Zhang and D. Aurbach, *Adv. Energy Mater.*, 2020, **10**, 2000697.
31 M. Lao, Y. Zhang, W. Luo, Q. Yan, W. Sun and S. X. Dou, *Adv. Mater.*, 2017, **29**, 1700622.
32 S. E. Sandoval, J. A. Lewis, B. S. Vishnugopi, D. L. Nelson, M. M. Schneider, F. J. Q. Cortes, C. M. Matthews, J. Watt, M. Tian and P. Shevchenko, *Joule*, 2023, **7**, 2054–2073.
33 H. Okamoto and C. B. Alcock, *J. Phase Equilib.*, 1991, **12**, 379–383.
34 V. P. Itkin and C. B. Alcock, *J. Phase Equilib.*, 1992, **13**, 162–169.
35 S. Tang, Z. Qiu, X.-Y. Wang, Y. Gu, X.-G. Zhang, W.-W. Wang, J.-W. Yan, M.-S. Zheng, Q.-F. Dong and B.-W. Mao, *Nano Energy*, 2018, **48**, 101–106.
36 S. Liu, Y. Ma, Z. Zhou, S. Lou, H. Huo, P. Zuo, J. Wang, C. Du, G. Yin and Y. Gao, *Energy Storage Mater.*, 2020, **33**, 423–431.
37 J. H. Lee, S.-H. Oh, H. Yim, H.-J. Lee, E. Kwon, S. Yu, J. S. Kim, J. Song, J. Koo and J. Cho, *Energy Storage Mater.*, 2024, **69**, 103398.